

# Ultra-High Gauge Factor Strain Sensor with Wide-Range Stretchability

Yogenth Kumaresan, Shashank Mishra, Oliver Ozioko, Radu Chirila, and Ravinder Dahiya\*

Strain sensors with wide-range stretchability, good sensitivity, high gauge factor, and reliability are needed for several applications. Herein, stretchable strain sensors capable of operating over multi-strain range and having an excellent gauge factor are presented. The systematic study, carried out with different combinations of elastomer, conductive filler, and graphene-carbon paste (GCP), revealed that the sensors exhibit excellent stretchability when only filler particles are present in the elastomer, and they exhibit high sensitivity when filler particles are mixed with GCP. The molecular dynamics simulations show that the addition of GCP to the elastomer-filler composite helps to attain an excellent sensor response with wide range stretchability. Thus, sensors' response can be tuned by using selected material composition. Accordingly, the strain sensor with 50 wt% GCP reveals 500% stretchability and a maximum gauge factor of 504. Likewise, 150 wt% GCP loading lead to sensors with 45% stretchability and an unprecedented gauge factor of 1 834 140. The capability to detect the small- to large-scale strains makes the presented sensors attractive for monitoring the movements of body parts—which range from small movements during facial expression to large movement experienced by the limb joints.

## 1. Introduction

There is a burgeoning demand for the real-time monitoring of strain to detect movements of humans and robot body parts via electronic skin<sup>[1]</sup> and wearable systems<sup>[2]</sup> for applications such as health monitoring,<sup>[3]</sup> human-robot interaction,<sup>[4]</sup> gaming, soft robotics,<sup>[5]</sup> and prosthesis.<sup>[3b,6]</sup> This has motivated the fabrication of several types of strain sensors with various materials, gauge factor, stretchability, and transduction mechanisms such as piezoresistive,<sup>[7]</sup> capacitive,<sup>[8]</sup> inductive,<sup>[9]</sup> and optical.<sup>[10]</sup> Among

these, the strain sensors based on the piezoresistive mechanism are popular due to their high sensitivity, ease of fabrication, diverse choice of materials, designs, and use in diverse environments and applications.<sup>[11]</sup> Stretchable piezoresistive-type strain sensors normally consist of a film of an active material (2D or 3D network of conductive material) fillers, which provide the conductive network and a stretchable polymeric substrate (e.g., Ecoflex and polydimethylsiloxane (PDMS)) for stretchability.<sup>[12]</sup> Commonly used conductive fillers in these sensors are based on graphene,<sup>[13]</sup> Carbon nanotubes (CNTs),<sup>[14]</sup> Ag nanowires,<sup>[15]</sup> ZnO,<sup>[16]</sup> carbon black,<sup>[17]</sup> graphite,<sup>[18]</sup> etc. Among these, the carbon-based filler materials are mostly used because of their abundant availability, cost-effectiveness, tunable electrical properties, large operational window, dispersibility in a variety of solvents, supporting matrix, and suitable mechanical features.

The sensitivity of a strain sensor is generally evaluated with gauge factor (GF), which is the ratio of the percentage change of sensor response to the applied strain. Strain sensors with the stretchability of the order of several hundred percent of the linear strain and sensitivity ranging from <10 to the order of 1000 have been reported for various applications.<sup>[3a,5,11]</sup> The material type, morphology of the active region, and the interaction of filler particles in that region are key to the response of the strain sensor. However, the majority of the works have mainly reported strain sensors with a specific figure of merit (e.g., gauge factor, stretchability, etc.) without systematically investigating how the modification of the active materials (the conducting composite) could modulate the response of the strain sensor. Further, it is highly challenging to have good sensitivity in high and low strain to accurately detect/identify large and small deformations.

Herein, we present strain sensors realized by combining different piezoresistive materials (CNT and graphite as conducting fillers and graphene-carbon paste (GCP)) in an elastomer matrix (Ecoflex) to achieve a high sensor response with a wide range of stretchability suitable for detecting large and small deformations by changing the filler composition. Three major combinations (elastomer-filler, GCP-filler, GCP-elastomer-filler) of these piezoresistive sensing materials realized by mixing the elastomer,

Y. Kumaresan, S. Mishra, O. Ozioko, R. Chirila, R. Dahiya  
Bendable Electronics and Sensing Technologies (BEST) Group  
University of Glasgow  
Glasgow G12 8QQ, UK  
E-mail: ravinder.dahiya@glasgow.ac.uk

The ORCID identification number(s) for the author(s) of this article can be found under <https://doi.org/10.1002/aisy.202200043>.

© 2022 The Authors. Advanced Intelligent Systems published by Wiley-VCH GmbH. This is an open access article under the terms of the Creative Commons Attribution License, which permits use, distribution and reproduction in any medium, provided the original work is properly cited.

DOI: 10.1002/aisy.202200043

conductive fillers (CNT and/or graphite), and graphene carbon paste have been investigated. The sample with the elastomer–filler combination exhibits excellent stretchability with moderate response. Meanwhile, the sensor with a GCP–filler combination revealed excellent sensor response with poor stretchability due to the fragmentation induced by GCP. However, an excellent sensor response with various ranges of stretchability was achieved after the introduction of GCP in the elastomer–filler combinations (GCP–elastomer–filler) because the elastomer–filler provides a percolation path to bridge the paste fragments under large strain. The same behavior was evident in our molecular dynamics (MD) simulation study. This systematic study helps to understand the role of three different types of fillers and shows how the sensor response can be tuned. For example, the higher CNT content tends to increase the stretchability, but the random entanglement of CNT decreases the performance of the strain sensor (poor gauge factor). Similarly, for composite with graphite only, the higher graphite content is needed to achieve a conductive path, which also hinders the stretchability and performance. The optimized amount of graphite, CNT, and GCP revealed better performance in terms of stretchability, response time, reliability, long-term stability, and hysteresis in comparison with previously developed stretchable strain sensors.<sup>[19]</sup> Interestingly, the sensor reveals stretchability from 0 to 625% strain with the gauge factor from 0.8 to 1834 140. In addition, the sensors exhibited stable response when attached to the human skin for human motion detection.

## 2. Result and Discussion

**Figure 1** shows the fabrication process of the piezoresistive strain sensor that has a multilayered structure with a piezoresistive sensing layer sandwiched between the two layers of thin Ecoflex that act as a substrate and an encapsulation layer. Three different composite materials (elastomer–filler, GCP–filler, and elastomer–GCP–filler) comprising of different piezoresistive sensing layers realized using different combinations of carbon filler materials (CNT, and/or graphite), Ecoflex, and GCP were investigated. In the case of elastomer–filler composite, the conductive path is achieved through the continuous network of the filler particles in the insulating elastomer matrix. There are two important parameters that govern the conduction path formation—the proper dispersion of filler inside the elastomer matrix and the loading weight percentage (wt%) of filler particles. For example, the agglomeration of filler particles leads to uneven distribution inside the elastomer matrix, which results in a highly conductive network at the agglomerated site and insulating at the others. The observation of structural morphology using the scanning electron microscope (SEM) is one of the simplest ways to understand the distribution of filler particles inside the elastomer matrix. **Figure 2** shows the SEM image of CNT, graphite, Ecoflex–graphite–CNT composite, and Ecoflex–GCP–CNT–graphite. In general, filler particles are attracted to each other due to van der Waals forces in the agglomeration (**Figure 2a,b**). To achieve uniform distribution of filler particles inside the elastomer matrix, CNTs of suitable weight percent (wt%) were added to the Ecoflex Part A and continuously mixed/sonicated for 5 min. Likewise, the graphite

microparticles were added to Ecoflex Part B and sonicated. Finally, both Part A and Part B were mixed together to obtain elastomer–filler composite. It can be observed from the SEM image that the fillers such as CNTs and graphite particles are uniformly distributed along the insulating matrix as shown in **Figure 2c,f**. Further, the X-Ray diffraction (XRD) was performed to evaluate the filler loading inside the elastomer, as shown in **Figure S1a**, Supporting Information. The two peaks at  $2\theta = 28^\circ$  (002) and  $2\theta = 44^\circ$  (100) in the XRD reflect strong carbon diffraction from filler particles (the graphite, CNT, and GCP). This indicates that the filler particles have been embedded inside ecoflex.<sup>[20]</sup>

To understand the network formation of elastomer–filler composition, samples (length  $\times$  width  $\times$  height = 3.5 cm  $\times$  0.5 cm  $\times$  0.1 mm), we evaluated different loading percentage of fillers. The resistance values of the samples measured using a digital multimeter across the two extreme corners are tabulated in **Figure S1b**, Supporting Information. The specific filler loading at which the conductive network is formed in the elastomer matrix is called the percolation threshold. At the percolation threshold, the filler particles may not be in direct contact with one another, and the electrons are mainly transported through tunneling. In general, the maximum tunneling distance to achieve continuous electron transportation has been reported to be less than 5 nm.<sup>[21]</sup> With a small amount of filler particles, there are very few conductive paths available and as a result, the resistance across the device is high with a value ranging from a few tens of k $\Omega$  to M $\Omega$ . As shown in **Figure 2d**, the graphite: CNT loading of either 10:1.5 or 20:0 ratio resulted in a high resistance value of 40 k $\Omega$ . Further, working close to the percolation threshold creates signal fluctuation because a small strain can disrupt the conductive network and substantially affect the resistance. When the loading is lower than the percolation threshold, the filler particles are not continuous and there is no conduction path along the filler, no electron flow, which makes the composite insulating. Accordingly, only graphite (up to 10 wt%) or only CNT (up to 2 wt%) revealed insulating behavior (**Figure 2d**). In contrast, with higher loading, i.e., above the percolation threshold, the filler particles come in direct contact with each other and form a connected network, which allows the formation of a highly conductive (low resistance) path. Accordingly, the loading of both graphite (>10 wt%) and CNT (>1.5 wt%) filler particles above their percolation threshold revealed a good conductive network with the resistance value ranging from 200  $\Omega$  to 6 k $\Omega$  (**Figure S1c**, Supporting Information). Further increase in the filler loading, especially the loading of >20 wt% graphite or 3 wt% CNT, and/or the combination of >10 wt% Graphite and >2 wt% CNT make it difficult to have uniform distribution or cure the elastomer–filler composite.

Based on these observations, we fabricated elastomer–filler composites with two different mixing ratios of elastomer: graphite: CNT, 10:1:3 (named as Sample 1) and 10:2:1.5 (Sample 2), and their sensing performance under different stretching were measured as shown in **Figure 3**. In general, the strain sensor with excellent stretchability and high gauge factor is obtained either by the generation of intentional or unintentional microcracks.<sup>[22]</sup> Phenomenological models also predict that the voltage distribution in crack-based strain sensors drops much faster than in flat sensors.<sup>[23]</sup> This means a greater resistance change is

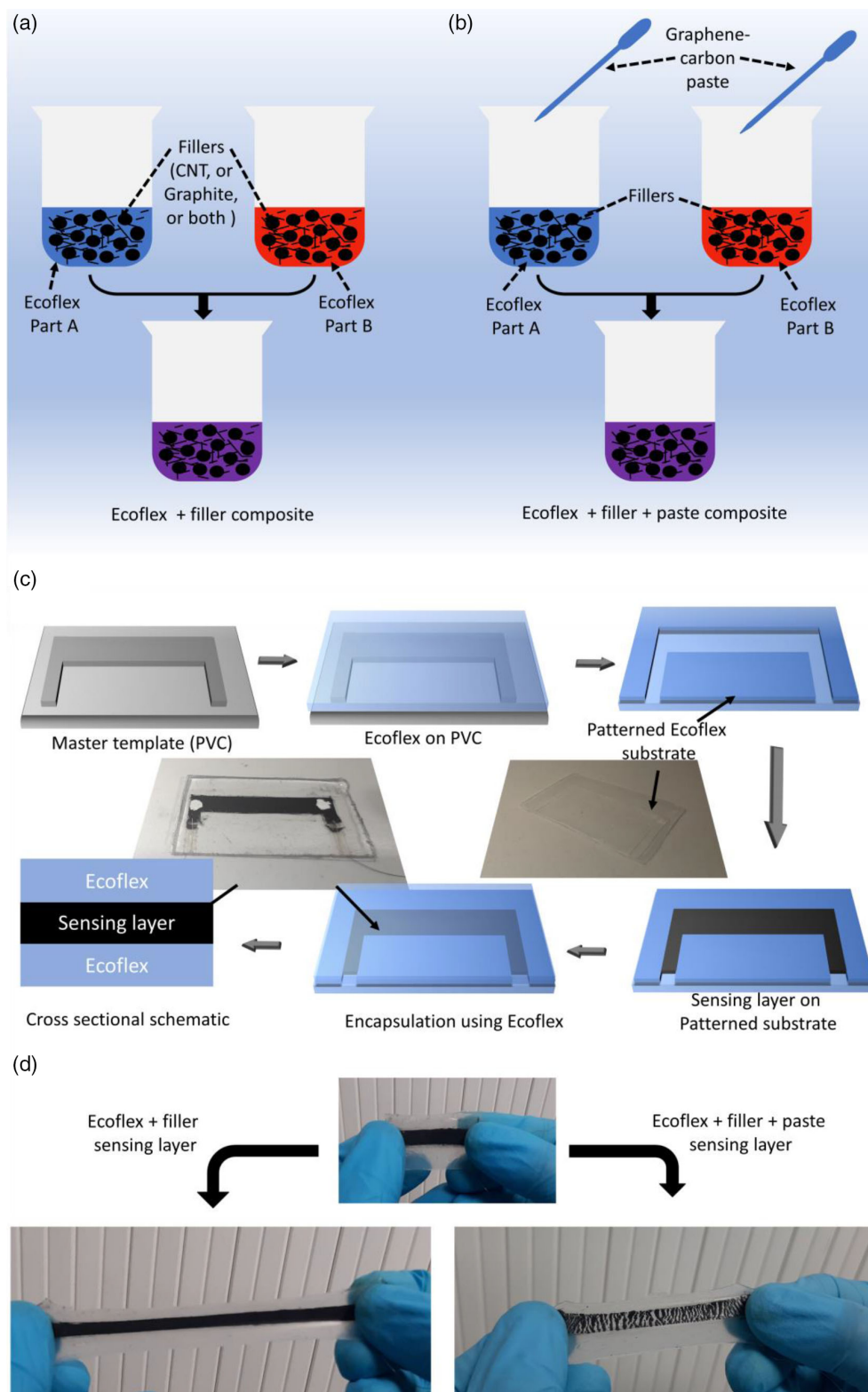


**Figure 1.** Schematic representation of the synthesis and fabrication process for stretchable strain sensor: a–b) Synthesis of strain sensing materials, namely Ecoflex + filler composite: a) without graphene–carbon paste (GCP) and b) with GCP; c) Fabrication steps of stretchable strain sensors including master template preparation, casting Ecoflex, separation of patterned Ecoflex substrate, coating sensing layer using doctor blade technique and encapsulating using Ecoflex, photographic image of patterned Ecoflex substrate and the stretchable strain sensor is shown in the inset; d) A photographic image of the sensor without GCP and with GCP under stretching.

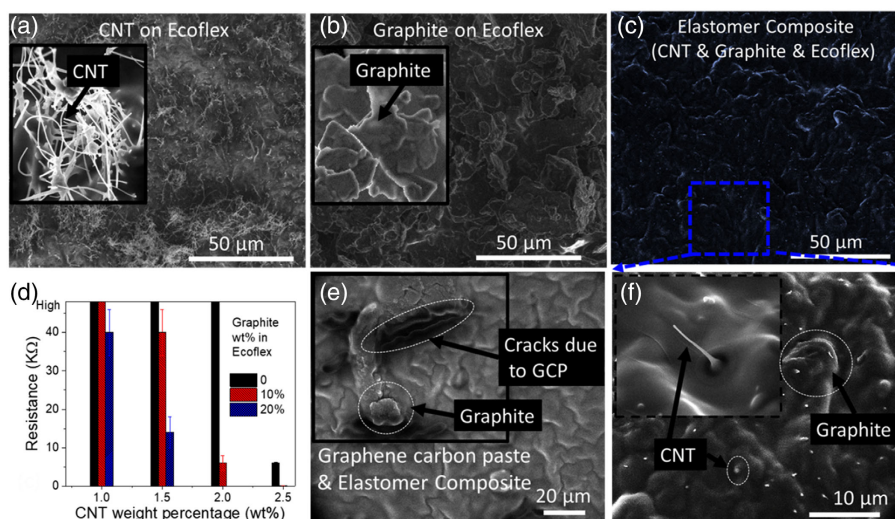


**Figure 2.** Surface morphology of the filler particles inside elastomer matrix and their electrical characteristics. Scanning electron microscope (SEM) image of: a) CNT on Ecoflex, b) graphite particles on Ecoflex, and c) elastomer filler made of Ecoflex–CNT–graphite. d) The resistance value with respect to different CNTs and graphite loading wt% inside the Ecoflex. SEM image of elastomer composite: e) with GCP and f) without GCP.

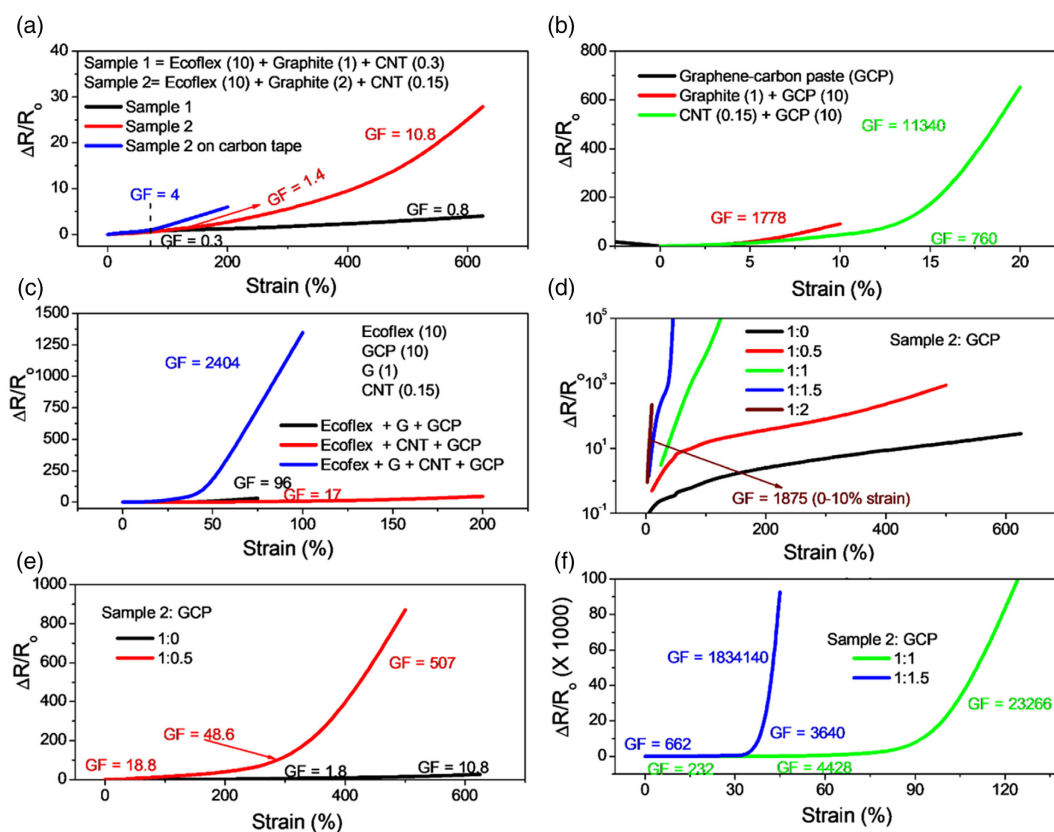


**Figure 3.** Comparison of strain sensor performance with different combinations of sensing channels made from elastomer–filler, paste–filler, and elastomer–paste–filler. The relative change in resistance under various stretching for: a) elastomer–filler composite, b) GCP–filler composite, and c) elastomer–GCP–filler composite. d–f) The comparison of sensor performance with different loading of paste (GCP) to Sample 2: d) Logarithmic plot for all combinations; e) linear plot highlighting 1:0 and 1:0.5 ratio of Sample 2: GCP; f) Linear plot highlighting 1:1 and 1:1.5 ratio of Sample 2: GCP.

expected during stretching. Therefore, we introduced an equal amount of GCP (details are given in the experimental section

and Figure S2, Supporting Information) to Sample 2 with the mixing ratio of 1:1 (Sample 2:GCP). The surface profile

measured using SEM before and after mixing the paste is given in Figure 2e,f. It is clear that the surface of the GCP: elastomer composite demonstrated numerous cracks and boundaries. The electrical property of different combinations of sensing channels including elastomer–filler, GCP–filler, and elastomer–GCP–filler are given in Figure 3. For better understanding, the flow of various combinations of samples used in this study is described in Figure S2a, Supporting Information.

As the combination of elastomer and one type of filler particles demonstrated insulating behavior, the sensing performance of three different combinations of elastomer–filler composite has been explored by placing the elastomer filler composites on patterned-carbon tape (Figure S2b, Supporting Information, describes the device architecture). The detailed mixing ratio of various sensing materials and their sensor response are tabulated in Figure S2c, Supporting Information. The sensor response was characterized by measuring the change in resistance while stretching the sensors from 0 to 625% strain. As shown in Figure 3a, Sample 1 and Sample 2 are highly stretchable (625%) with the gauge factor ranging from 0.3 to 10.4 at different stretching ranges. Sample 2 coated on patterned-carbon tape revealed 200% stretchability with a maximum gauge factor of 4, but the sensing channel got completely disconnected above 200% stretching. This is because the carbon tape tends to create cracks/separation when subjected to external stretching. Interestingly, at a low stretching range below 200%, Sample 2 on patterned-carbon tape demonstrated the highest gauge factor among all the three samples. In contrast, Samples 1 and 2 revealed excellent stretchability (625%). Additionally, the GCP–filler composites were explored by fabricating three combinations, namely only GCP, graphite filler in GCP, and CNT filler in GCP. The sample with only GCP was not stretchable as there was no flow of electrons when subjected to more than 1% strain as shown in Figure 3b. The addition of filler particles inside the GCP paste helps to maintain the flow of electrons up to 20% strain. In comparison with the graphite particles, the sample with CNT demonstrated much higher stretchability up to 20% strain with a gauge factor of  $\approx 11\,340$ .

It is worth mentioning that the elastomer–filler particles revealed excellent stretchability but were limited in their change in response and the gauge factor. At the same time, the paste–filler composite demonstrated exactly the opposite behavior with low stretchability and excellent sensor response/gauge factor. From the results, we expect that the combination of the elastomer and filler particle complements each other to achieve both the stretchability and the sensor response. Accordingly, three combinations of the sensors were fabricated by adding different filler particles, namely graphite, CNT, and CNT + graphite, in the GCP–elastomer matrix and the sensor response was characterized as shown in Figure 3c. Here, the addition of CNT filler in the GCP–elastomer matrix revealed good stretchability (>200%) but the change in resistance under different stretching is very low (gauge factor of 0.8). Likewise, the addition of graphite particles enhanced the gauge factor from 0.8 to 96 but the stretchability is limited to 75%. This is because the GCP has the tendency to create a void or cracks inside the GCP–elastomer matrix and the graphite particles have the tendency to separate from each other along the cracks resulting in the discontinuity of the continuous path. In contrast, the

CNTs entangle with each other and act as a bridge between the generated GCP islands while stretching. Interestingly, the elastomer–paste–filler given in Figure 3c revealed an enhanced sensor response, in comparison with the elastomer–filler (Figure 3a) and GCP–filler (Figure 3b), with the maximum gauge factor of  $\approx 2404$  and the change in resistance of  $\approx 1400$  at 100% strain. Here, the combination of graphite and CNT filler particle complement each other to achieve superior sensor response with excellent stretchability.

For better understanding, five set of devices were fabricated with different GCP ratios in Sample 2 (0 wt% GCP-1:0, 50 wt% GCP- 1:0.5, 100 wt% GCP- 1:1, 150 wt% GCP- 1:1.5, and 200 wt% GCP- 1:2) and their change in resistance to the strain is plotted in Figure 3d–f. Further, the sensor response (gauge factor) from Figure 3d is plotted separately in Figure 3e,f. It is clearer that the stretchability of the sensor decreased and the change in resistance value increased with the addition of GCP. For example, the addition of 50 wt% GCP to Sample 2 tends to decrease the stretchability from 625% to 500% while the gauge factor value increased from 10.8 to 570 (Figure 3e). Likewise, increasing the GCP loading to 100 and 150 wt% resulted in a further decrease in stretchability (125% to 45%) with a dramatic increase in the gauge factor value (23 366 to 1 834 140) as shown in Figure 3f. The hysteresis behavior was systematically studied by adding different ratios of GCP to Sample 2 (Figure S3a–d, Supporting Information). The GCP is generally nonelastic in nature with numerous grain boundaries which could separate under external stretching. As a result, GCP is more likely to separate into small islands, which could drastically reduce the conductive paths and increase the resistance of the film. When the external stress is removed, the separated islands once again come in contact with each other and form the conductive paths almost similar to the pristine film. We observed a similar trend with increasing GCP content in Sample 2. The addition of GCP enhanced the sensor performance and reduced the hysteresis.

The real-time sensor response with systematic stretching and releasing cycles at various strain values was performed, for 100 wt% GCP and 150 wt% GCP samples, to evaluate the response time and reliability. In each cycle, the resistance value was continuously measured when the sensor was stretched and held for 15 s followed by a release for another 15 s at various stretching strains as shown in Figure 4a,b. In both samples, the resistance value abruptly increased from its base value when subjected to external strain with a relative change in resistance value reaching a maximum of  $\approx 10^5$ . It is worth mentioning that the sensors demonstrated a fast response time (0.4 s) and recovery time (0.3 s) as shown in Figure 4c. Further, the sensor revealed a stable sensor response with the resistance value returning to the base line in less than a minute when subjected to a 10 s stretch-and-release cycle for over 1200s (Figure 4d). The sensors with and without 150 wt% GCP loading, preserved for six months, were subjected to 750 stretching cycles at 200% strain and 40% strain, respectively. Interestingly, the performance of the sensor (relative change in resistance) was found to be stable even six months after the fabrication (Figure S4a,b, Supporting Information). The response of the five sensing devices was found to be reproducible with a standard deviation of less than 5% (Figure S5, Supporting Information). The stretchability

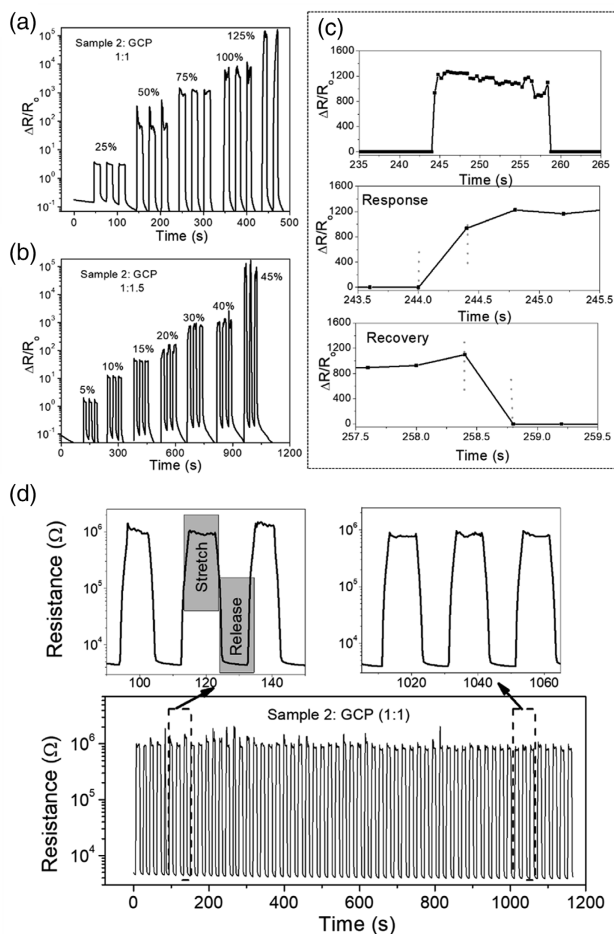


**Figure 4.** Real-time electromechanical characteristics of elastomer-GCP-filler composite: The relative change in resistance under systematic stretching cycles (15 s each) under various strains for sensors made of: a) 100 wt% GCP loading with Sample 2 and b) 150 wt% GCP loading with Sample 2; c) The magnified sensor response extracted from Figure 4a highlighting the sensors response and recovery time; d) Real-time resistance change under systematic stretch and release cycle of 10 s each for 1200 s for 100 wt% GCP loading in Sample 2.

decreased with GCP loading, as a result, the sensor with the 100 wt% GCP loading reaches its maximum relative change in resistance value ( $10^5$ ) at 125% strain but the sensor with the 150 wt% GCP loading reaches a much lower strain (45%). To understand the role of GCP in sensor response and stretchability, we performed molecular dynamics (MD) simulations on the elastomer matrix before and after adding the GCP.

**Figure 5** shows the simulation results of both composites i.e., with and without GCP at various strains. It can be clearly seen that the composite having GCP shows voids at a strain level of  $\approx 70\%$ , which leads to cracking in the composite at 110% strain. Whereas composite without GCP shows no cracking behavior even at 110% strain. As the graphene and carbon black in the GCP tends to increase the density of fillers inside the elastomer matrix, there is a high particle to particle interactions due to weak van der Waals forces resulting in agglomeration. It is clearly evident from the supporting video (Video SV1,

Supporting Information) that microcracks were generated perpendicular to the stretching axis. As a result of numerous cracks, the available conducting paths decreased with the strain. Accordingly, the relative change in resistance value dramatically increased with higher GCP loading, as shown in Figure 3d. However, the sample without GCP or less loading of GCP has a relatively small change in resistance due to the availability of more conductive paths in comparison with its counterpart. The observation made from the simulation matched with our experimental results that the addition of GCP contributed to the decrease in stretchability and increase in sensor response (Figure 3d).

To evaluate the performance of our sensor for real-life applications in wearable systems, we attached the elastomer-GCP-filler-based sensor to various parts of the human body using biocompatible tapes and monitored a wide range of human motions, which included small stretching actions such as smiling to large stretching actions as in joint movements. First, three different strain sensors, obtained by varying the GCP loading, namely 50, 100, and 150 wt%, in Sample 2 were attached to the proximal-interphalangeal joints of the index finger and their resistance value was measured using a multimeter for different cyclic bending motions as shown in **Figure 6a–c**. It is clearer that the base resistance value decreased with an increase in the GCP loading and the resistance change under bending is very high. For example, in case of 150 wt% GCP loading, the base resistance value drastically increased from  $\approx 1.5$  k $\Omega$  to  $\approx 25$  M $\Omega$  with a change in the resistance value of  $\approx 10^4$ . At the same time, the sensor made of 50 wt% GCP loading demonstrated a small relative change in the value of 3.26 in which the base resistance value changed from  $\approx 15$  to  $\approx 64$  k $\Omega$ . It is worth mentioning that the sensors with GCP loading revealed a stable response with quick response/recovery time and reached their initial base value in less than a minute (Figure 6a–c).

The sensor made of 100 wt% GCP loading was attached to different joints, namely proximal-interphalangeal joints, metacarpophalangeal joints, wrist joints, and elbow, and their sensor response was monitored. As shown in Figure 6d–g, the change in the resistance value was completely synchronized with the cyclic motion of human body parts and the robotic iLimb hand (Figure 6h). The 50 wt% GCP loading sensor was also attached to the iLimb robot hand, which was operated with three bending angles and the real-time resistance was measured. The iLimb prosthetic hand has no inherent control mechanism, and finger positions are currently determined internally solely using the current consumption of the motors. Therefore, the reliable way of controlling the angle of each finger was achieved using a software-based timed interrupt controller. The interrupt controller was responsible for sending “abort process” signals over the communication link between the computer and the prosthetic hand (CAN bus). The period of the cyclic test was set at 10 s. As shown in Figure 6e (Supporting Video SV2), the sensor revealed a reliable cyclic response with clearly distinguishable gestures under three conditions.

The sensor made of 150 wt% GCP attached to proximal-interphalangeal joints of a finger could be used to clearly identify the movement of the particular finger (Figure 6f). Further, the ability of sensors to detect small strains

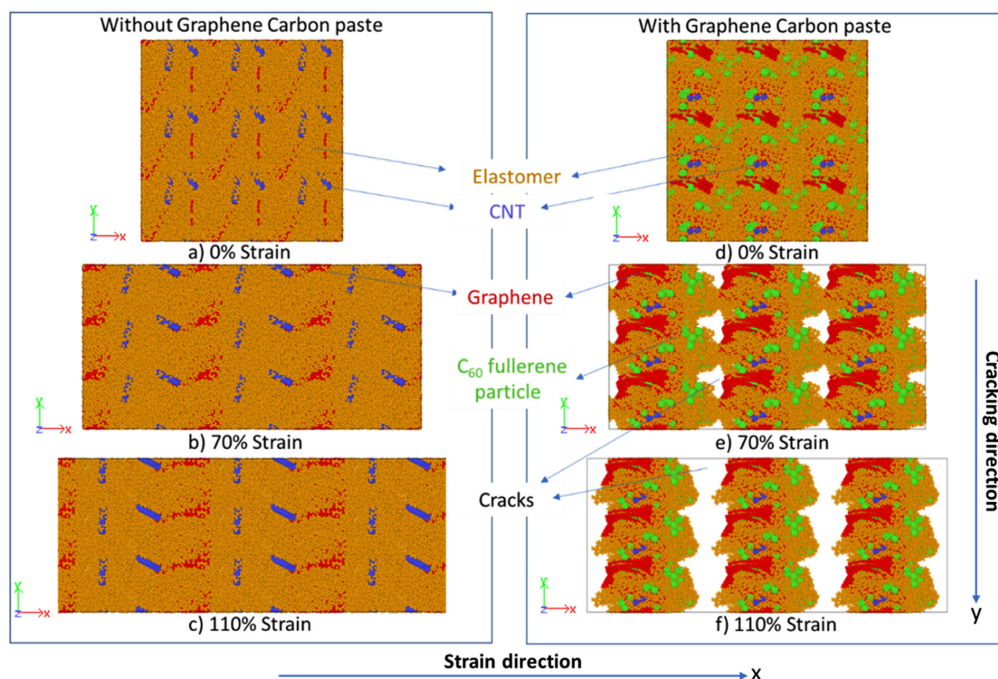


**Figure 5.** Snapshots from molecular dynamics simulation for elastomer–GCP–filler composite: a,b,c) without GCP and d,e,f) with GCP.

to large moments was tested as shown in Figure S6, Supporting Information. The sensor with 100 wt% GCP loading was attached to the cheek for small deformation detection. Under periodic smiling expression, the resistance value of the sensor changed from 2.7 to 8 k $\Omega$  with the change in  $\Delta R/R_0$  of 2, which is smaller in comparison with the joint movements ( $\Delta R/R_0 \approx 70$  for ulno-humeral joint movement). At the same time, the sensor with higher GCP loading (150 wt%) exhibits a large change in resistance from 1.7 to 18 k $\Omega$  with  $\Delta R/R_0 \approx 10$  (Figure S6e,f, Supporting Information). However, decreasing the GCP loading lower than 100 wt% revealed no response for smiling expression. Likewise, increasing the GCP loading above 150 wt% is not effective for detecting/distinguishing the movement of joints. Therefore, the controlled addition of GCP helps to detect both small deformation and large stretching.

### 3. Conclusion

In summary, high-performance stretchable strain sensors with wide-range stretchability (0%–625% strain) and sensor response (0.8- to 1 834 140-gauge factor) were developed by optimizing the combining elastomer (Ecoflex), conductive fillers (CNT and graphite), and GCP. The sensor with the elastomer–filler combination revealed excellent stretchability but the relative change in resistance is small under stretching. Alternatively, the GCP–filler combination revealed excellent sensor response with the maximum gauge factor of 11 340 but the maximum stretchability (strain sensing range) is limited to 20% strain. Interestingly, the combination of GCP with the elastomer–filler composite demonstrated a wide range of stretchability with various ranges of gauge factors based on the material composition recipe. An

increase in GCP decreased the base resistance value and increased the change in resistance under stretching. The sensor was fabricated with the addition of 150 wt% GCP in the elastomer–filler composite revealed 45% stretchability, fast response and recovery, excellent sensor response with an unprecedented gauge factor of 1 834 140, and good stability over repeated cyclic measurement. The stable cyclic response of our sensors under various human motion demonstrate their suitability for various human–machine interface applications.

### 4. Experimental Section

**Synthesis of Strain Sensing Materials:** Three combinations of piezoresistive sensing materials, namely elastomer–filler, GCP–filler, and elastomer–GCP–filler were synthesized using elastomer (Ecoflex), paste (GCP), and filler (CNT and/or graphite). The desired amount of elastomer, paste, and filler (supporting information Figure S2c, Supporting Information) were mixed to achieve various combinations of piezoresistive sensing material. Figure 1a depicts the synthesis of elastomer–filler composite-based piezoresistive material. First, the filler particles such as CNTs (50–90 nm diameter and 6.7  $\mu\text{m}$  length) or graphite ( $\approx 40 \mu\text{m}$  diameter) were added separately to the Part A and Part B of the Ecoflex at desired wt% and manually stirred for 5 min to achieve uniform dispersion. Sequentially Part A and Part B were mixed for 5 min and immediately used for fabricating the elastomer–filler composite-based piezoresistive strain sensor as shown in Figure 1c. Almost similar steps were adopted to synthesize the elastomer–GCP–filler composite-based piezoresistive material in which the GCP was added and mixed, in addition to filler, prior to the mixing of part A and part B (Figure 1b). Likewise, in the case of paste–filler composite-based piezoresistive material, the desired amount of filler particles were directly added to the paste followed by 5 min manual mixing and sensor fabrication.

**Sensor Fabrication and Characterization Technique:** Figure 1c depicts the fabrication process of the piezoresistive strain sensor using the

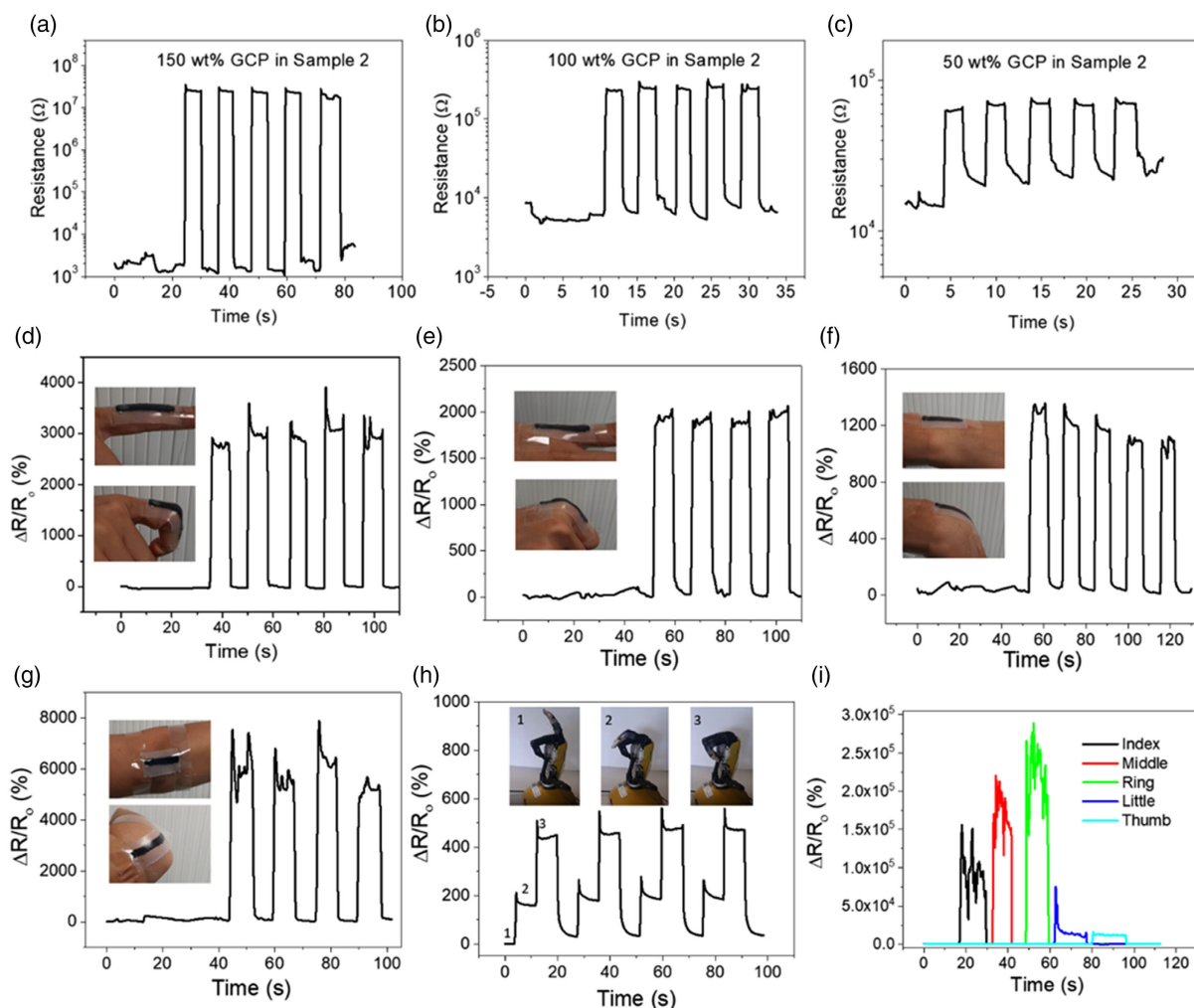


**Figure 6.** Wearable sensing device to monitor physical movement. a–c) The real-time resistance value of the sensors attached to proximal–interphalangeal joints subject to bending motion: a) Sensor with 150 wt% GCP in Sample 2; b) sensor with 100 wt% GCP in Sample 2; c) sensor with 50 wt% GCP in Sample 2. The change in resistance of sensor (100 wt% GCP in sample 2 device) when attached to different joints, namely d) proximal–interphalangeal joints, e) metacarpophalangeal joints, f) wrist joints, and g) elbow. h) The electromechanical response of the sensor (50 wt% GCP in sample 2 device) when attached to the Ossur iLimb Access Robotic Prosthetic Hand with three different fingers gesture. i) The response of the sensor (150 wt% GCP in sample 2 device) when attached to the proximal–interphalangeal joints of the five fingers.

mentioned materials. The strain sensor consists of three layers, namely the bottom substrate, sensing layer, and the encapsulation layer. First, the master mold with a  $3.5\text{ cm} \times 0.5\text{ cm} \times 175\text{ }\mu\text{m}$  (length, width, height) pattern was fabricated on polyvinyl chloride substrate using the blade cutter tool. Ecoflex was poured, cured, and separated from the master mold to realize a substrate with a  $175\text{ }\mu\text{m}$  thick pit containing the inverse pattern of the mold (Figure 1c). The piezoresistive sensing materials were uniformly coated inside the pit using the doctor blade technique. Following the curing of the sensing material, Ecoflex was used to encapsulate the sensing channel. Devices were characterized by clamping them in a custom-made stretching system consisting of two linear stage motors (VT-21 from Micronic USA) connected to the LabVIEW software driven by Pollux Box with the capability to precisely control the stage movement, as explained elsewhere.<sup>[6c]</sup> A digital multimeter (Keysight, 3446X) was used to record the resistance change. The SEM images were obtained using FEI Nova NanoSEM.

**Simulation Methodology:** To understand the reason behind the contrasting behavior of the strain sensors, MD simulations were run on these

sensor materials. In these simulations, first two systems were created with PDMS molecules acting as the elastomer material. In the first system, 100 chains of PDMS having 15 monomers each were taken in a box and then 2 graphene sheets (having size  $5\text{ nm} \times 5\text{ nm}$  with chirality (3,3) and 2 single-walled carbon nanotubes (SWCNT) (having tube length of 4.92 nm and a tube diameter of 0.41 nm with chirality (3,3) were added in this box in such a way that the weight ratio of 1:0.2:0.015 is maintained. In the second system, 4 graphene sheets and 60 C60 fullerene particles (to mimic the effect of spherical carbon particles present in GCP) were added additionally in the previous system. These extra graphene sheets and fullerene particles were added to mimic the GCP used in the experiment and the weight ratio was maintained as the same as in the experiments.

Both the systems were initially minimized, followed by number of particles, pressure, and temperature (NPT) equilibration at 0 atm pressure and 300 K temperature for 1 ns with a timestep of 1 fs. Then, these systems were subjected to simulated annealing from 300 K to 600 K with a total annealing time of 1 ns, and then they were relaxed at 600 K for another 1 ns. Further, they were cooled down to 300 K in another 1 ns

and finally, they were equilibrated at 300 K for 5 ns. Entire simulated annealing and equilibration were carried out in the NPT ensemble. Once equilibration was achieved, both systems were then subjected to a tensile test in the x-direction keeping the pressure in the other two directions at 0 atm with a strain rate of  $10^{10} \text{ s}^{-1}$ . All these simulations were run in LAMMPS<sup>28</sup> using OPLSAA forcefield parameters.

The experiments involving human subject have been performed with the full, informed consent of the volunteer.

## Supporting Information

Supporting Information is available from the Wiley Online Library or from the author.

## Acknowledgements

This work was supported in part by Engineering and Physical Sciences Research Council (EPSRC) through engineering fellowship for growth (EP/R029644/1) and European Commission through FET-OPEN project Ph-Coding (H2020-FETOPEN-2018- 829186) and Innovative Training Network Project INTUITIVE (H2020-MSCA-ITN-2019-861166).

## Conflict of Interest

The authors declare no conflict of interest.

## Author Contributions

Y.K and S.M equally contributed to this work. Y.K. and R.D.: conceived the original idea. Y.K., S.M., and O.O.: designed the experiments, fabricated and characterized the sensor. S.M.: performed the molecular dynamics simulation to explain the concept of crack generation after the addition of GCP in the elastomer–filler composite. R.C.: contributed to the demo by controlling the iLimb robot hand. All authors contributed to the manuscript writing. All authors have given approval to the final version of the manuscript. R.D.: provided overall supervision of the project.

## Data Availability Statement

The data that support the findings of this study are available from the corresponding author upon reasonable request.

## Keywords

carbon nanotubes, elastomer and gauge factor, strain sensors, stretchable electronics

Received: February 14, 2022

Revised: May 11, 2022

Published online: June 16, 2022

- [1] a) R. Dahiya, *Proc. IEEE* **2019**, *107*, 247; b) R. Dahiya, D. Akinwande, J. S. Chang, *Proc. IEEE* **2019**, *107*, 2011.  
 [2] O. Ozioko, R. Dahiya, *Adv. Intell. Syst.* **2022**, *4*, 2100091.  
 [3] a) P. Escobedo, M. Bhattacharjee, F. Nikbakhtnasrabadi, R. Dahiya, *IEEE Internet Things J.* **2021**, *8*, 5093; b) A. Pullanchiyodan,

- L. Manjakkal, M. Ntagios, R. Dahiya, *ACS Appl. Mater. Interfaces* **2021**, *13*, 47581.  
 [4] M. Bhattacharjee, M. Soni, P. Escobedo, R. Dahiya, *Adv. Electron. Mater.* **2020**, *6*, 2000445.  
 [5] P. Karipoth, A. Christou, A. Pullanchiyodan, R. Dahiya, *Adv. Intell. Syst.* **2022**, *4*, 2100092.  
 [6] a) H. Tai, Z. Duan, Y. Wang, S. Wang, Y. Jiang, *ACS Appl. Mater. Interfaces* **2020**, *12*, 31037; b) C. M. Boutry, Y. Kaizawa, B. C. Schroeder, A. Chortos, A. Legrand, Z. Wang, J. Chang, P. Fox, Z. Bao, *Nat. Electron.* **2018**, *1*, 314; c) P. Karipoth, A. Pullanchiyodan, A. Christou, R. Dahiya, *ACS Appl. Mater. Interfaces* **2021**, *13*, 61610.  
 [7] a) A. Georgopoulou, F. Clemens, *ACS Appl. Electron. Mater.* **2020**, *2*, 1826; b) P. K. Dubey, N. Yogeswaran, F. Liu, A. Vilouras, B. K. Kaushik, R. Dahiya, *IEEE Trans. Electron Devices* **2020**, *67*, 2140.  
 [8] A. Atalay, V. Sanchez, O. Atalay, D. M. Vogt, F. Haufe, R. J. Wood, C. J. Walsh, *Adv. Mater. Technol.* **2017**, *2*, 1700136.  
 [9] M. Tavassolian, T. J. Cuthbert, C. Napier, J. Peng, C. Menon, *Adv. Intell. Syst.* **2020**, *2*, 1900165.  
 [10] G. Kamita, B. Frka-Petesic, A. Allard, M. Dargaud, K. King, A. G. Dumanli, S. Vignolini, *Adv. Opt. Mater.* **2016**, *4*, 1950.  
 [11] a) L. Duan, D. R. D'hooge, L. Cardon, *Prog. Mater. Sci.* **2020**, *114*, 100617; b) H. Souri, H. Banerjee, A. Jusufi, N. Radacsi, A. A. Stokes, I. Park, M. Sitti, M. Amjadi, *Adv. Intell. Syst.* **2020**, *2*, 2000039.  
 [12] a) R. Dahiya, M. Valle, in *Robotic Tactile Sensing: Technologies and System*, Springer Science + Business Media, Dordrecht **2013**.  
 b) X. Fu, A. M. Al-Jumaily, M. Ramos, A. Meshkinzar, X. Huang, *J. Biomater. Sci. Polym. Ed.* **2019**.  
 [13] S. W. Lee, J. J. Park, B. H. Park, S. C. Mun, Y. T. Park, K. Liao, T. S. Seo, W. J. Hyun, O. O. Park, *ACS Appl. Mater. Interfaces* **2017**, *9*, 11176.  
 [14] Y. Gao, X. Fang, J. Tan, T. Lu, L. Pan, F. Xuan, *Nanotechnology* **2018**, *29*, 235501.  
 [15] M. Amjadi, A. Pichitpajongkit, S. Lee, S. Ryu, I. Park, *ACS Nano* **2014**, *8*, 5154.  
 [16] Q. Chen, Y. Sun, Y. Wang, H. Cheng, Q.-M. Wang, *Sens. Actuator A Phys.* **2013**, *190*, 161.  
 [17] W. Zhai, Q. Xia, K. Zhou, X. Yue, M. Ren, G. Zheng, K. Dai, C. Liu, C. Shen, *Chem. Eng. Technol.* **2019**, *372*, 373.  
 [18] W. Li, J. Guo, D. Fan, *Adv. Mater. Technol.* **2017**, *2*, 1700070.  
 [19] a) J. Shintake, Y. Piskarev, S. H. Jeong, D. Floreano, *Adv. Mater. Technol.* **2018**, *3*, 1700284. b) M. Amjadi, Y. J. Yoon, I. Park, *Nanotechnology* **2015**, *26*, 375501. c) T. Xiao, C. Qian, R. Yin, K. Wang, Y. Gao, F. Xuan, *Adv. Mater. Technol.* **2021**, *6*, 2000745. d) M. Nankali, N. M. Nouri, M. Navidbakhsh, N. Geran Malek, M. A. Amindehghan, A. Montazeri Shahtoori, M. Karimi, M. Amjadi, *J. Mater. Chem. C* **2020**, *8*, 6185.  
 [20] a) V. Selen, Ö. Güler, D. Özer, E. Evin, *Desalin. Water Treat.* **2016**, *57*, 8826–8838. b) Y. Zhang, E. Ren, H. Tang, A. Li, C. Cui, R. Guo, M. Zhou, S. Jiang, H. Shen, *J. Mater. Sci.: Mater. Electron.* **2020**, *31*, 14145.  
 [21] Y. Zare, K. Y. Rhee, *J. Mater. Res. Technol.* **2020**, *9*, 15996.  
 [22] Z.-Y. Li, W. Zhai, Y.-F. Yu, G.-J. Li, P.-F. Zhan, J.-W. Xu, G.-Q. Zheng, K. Dai, C.-T. Liu, C.-Y. Shen, *Chinese J. Polym. Sci.* **2021**, *39*, 316.  
 [23] a) Y. Liu, H. Fan, K. Li, N. Zhao, S. Chen, Y. Ma, X. Ouyang, X. Wang, *Adv. Mater. Technol.* **2019**, *4*, 1900309; b) Y. Liu, Z. Sheng, J. Huang, W. Liu, H. Ding, J. Peng, B. Zhong, Y. Sun, X. Ouyang, H. Cheng, X. Wang, *Chem. Eng. J.* **2022**, *432*, 134370.